

---

# FIMP: FOUNDATION MODEL-INFORMED MESSAGE PASSING FOR GRAPH NEURAL NETWORKS

---

Syed Asad Rizvi<sup>1</sup>, Nhi Nguyen<sup>1</sup>, Haoran Lyu<sup>2</sup>, Benjamin Christensen<sup>1</sup>, Josue Ortega Caro<sup>3</sup>, Antonio H. O. Fonseca<sup>4</sup>, Emanuele Zappala<sup>5</sup>, Maryam Bagherian<sup>6</sup>, Christopher Averill<sup>7</sup>, Chadi G. Abdallah<sup>7</sup>, Amin Karbasi<sup>1,8</sup>, Rex Ying<sup>1</sup>, Maria Brbic<sup>9</sup>, Rahul M. Dhodapkar<sup>10,\*\*</sup>, and David van Dijk<sup>1,3,4,11,\*\*</sup>

<sup>1</sup>Department of Computer Science, Yale University

<sup>2</sup>Massachusetts Institute of Technology

<sup>3</sup>Wu Tsai Institute, Yale University

<sup>4</sup>Interdepartmental Neuroscience Program, Yale University

<sup>5</sup>Department of Mathematics and Statistics, Idaho State University

<sup>6</sup>University of Massachusetts Boston

<sup>7</sup>Baylor College of Medicine

<sup>8</sup>Google Research

<sup>9</sup>Swiss Federal Institute of Technology (EPFL)

<sup>10</sup>University of Southern California

<sup>11</sup>Internal Medicine, Yale University

\*\*Co-last Author, Corresponding Authors: rahul.dhodapkar@med.usc.edu, david.vandijk@yale.edu

## ABSTRACT

Foundation models have revolutionized the landscape of Deep Learning (DL), serving as a versatile platform which can be adapted to a wide range of downstream tasks. Despite their adaptability, applications of foundation models to downstream graph-based tasks have been limited, and there remains no convenient way to leverage large-scale non-graph pretrained models in graph-structured settings. In this work, we present a new framework which we term Foundation-Informed Message Passing (FIMP) to bridge the fields of foundational models and GNNs through a simple concept: constructing message-passing operators from pretrained foundation model weights. We show that this approach results in improved performance for graph-based tasks in a number of data domains, allowing graph neural networks to leverage the knowledge of foundation models.

## 1 Introduction

Transformer-based foundation models have emerged as a new paradigm of generalized Deep Learning (DL) models. Through large-scale pretraining on vast amounts of data, foundation models achieve a broad base of knowledge which can be effectively adapted to a wide range of downstream tasks [1]. Pretraining is typically done in self-supervised fashion through objectives such as autoregressive language modeling [2] and masked language/image modeling [3, 4], resulting in foundation models with generalized knowledge of vast amounts of data with minimal supervision required. Standard foundation models have emerged in fields such as Natural Language Processing (NLP) with BERT [3], GPT-3 [5], and CLIP [6], as well as in Computer Vision (CV) [7]. These models exhibit strong transfer to downstream applications after finetuning, outperforming task-specific models after pretraining on task-relevant unlabeled data [8]. More recently, fields such as single-cell RNA sequencing and neuroscience have seen the emergence of large-scale foundation models with scGPT [9], Geneformer [10], and BrainLM [11].

Despite their versatility, applications of foundation models to downstream tasks on graphs has been limited. Traditional Graph Neural Networks (GNNs) typically represent nodes using singular feature vectors, limiting their compatibility with transformer-based pretrained models which typically operate over tokenized sequences of features. Foundational models have been proposed for GNNs by adapting pretraining techniques to graph-structured settings [12], however the approach taken has been to train new foundation models from scratch on graph data, rather than adapting existing

foundation models to operate in a graph setting. The latter approach would unify the knowledge learned over large-scale non-graph pretraining, and would greatly increase opportunities for cross-domain training and transfer learning.

To address this, we propose FIMP, a method for constructing effective message-passing operators for graph settings using pretrained foundation model weights. Node features are encoded using data-dependent tokenization schemes, resulting in node feature sequences which can be ingested by transformer-based foundation models. Message-passing is then performed by adapting the attention layers from foundation models to perform cross-node multihead attention between feature sequences of neighboring nodes. This approach leverages the knowledge of foundation models to construct messages between nodes in a graph setting, greatly expanding the opportunities for utilizing foundation models in graph-based tasks. We benchmark FIMP against strong baseline GNN models on two biological application datasets, namely fMRI brain activity recordings and spatial transcriptomics datasets, as well as on an image graph dataset constructed from the Cifar-100 image dataset [13]. FIMP demonstrates strong performance, outperforming baselines by 28.6% on fMRI recording reconstruction and up to 18.6% on spatial genomics datasets, illustrating the benefits of adapting foundation models for message-passing in graph settings.

## 2 Related Works

### 2.1 Foundation models

Modern foundation models originated with the Transformer paper [14], which proposed the self attention-based architecture which now underpins many foundation models. Follow-up works such as BERT [3] and GPT [2] proposed general language modeling objectives, such as autoregressive and masked language modeling, for large-scale pretraining. Subsequent works scaled up the amount of data and compute given to the pretraining phase, giving rise to zero-shot and few-shot capabilities in GPT-2 [15] and GPT-3 [5]. Concurrently, CLIP [6] utilized contrastive learning on paired image and language data from the web, learning effective image and text representations which could be used for a wide variety of downstream multimodal tasks. Increasing compute, data, and pretraining techniques have given rise to more modern foundation language models, such as LLama-2 [16].

In Computer Vision (CV), works such as DINO [17] and MoCo [18] explored large-scale pretraining on image data, exhibiting emergent properties in transformer-based models trained at large scale. The Swin Transformer [19] architecture was proposed as a general-purpose backbone for CV-related tasks.

### 2.2 Graph foundation models

Many foundation GNN models utilize message-passing GNNs as their backbone architecture, while scaling up pretraining data in various domains to achieve a foundational model. Many initial works adapted self-supervised learning strategies from other fields into the graph domain as pretraining objectives. GraphCL [20] and GRACE [21] generated views of input graphs using data augmentation, performing contrastive learning between graph view representations. DGI [22] uses a discriminator network to maximize mutual information between node-level and graph-level embeddings. Newer lines of work adapt transformer models to graph learning tasks by representing an entire graph as a sequence of tokens, each representing a node in the graph. Transformer models provided a more expressive architecture for graph learning tasks, however new positional and structural encodings were necessary to properly encode a graph. General, Powerful, Scalable (GPS) Graph Transformer [23] proposed a recipe for constructing strong graph transformer architectures at scale, while dealing with the quadratic complexity of the attention mechanism. We note that while these works did apply transformer models to graphs, they were limited to operating on sequencings of tokens representing nodes, and could not tokenize simpler feature units within nodes.

More recent works have explored using Large Language Models (LLMs) in graph settings. GPT4Graph [24] examined the proficiency of LLMs in understanding graph structure converted into text format, demonstrating several potential tasks using LLMs in graph settings with prompt finetuning. NLGraph [25] proposed a benchmark for LLM reasoning over graphs, and further developed two prompting approaches to improve LLM reasoning over graph questions in natural language. While these works utilize pretrained LLMs for graph tasks, we note that it is different than our work in that these methods are limited to converting graph problems into text and using pretrained LLMs to conduct reasoning in natural language format. Our goal is to open the possibility for any foundation model from any pretraining domain to be converted into an effective message-passing operator for direct application on graph-structured settings.

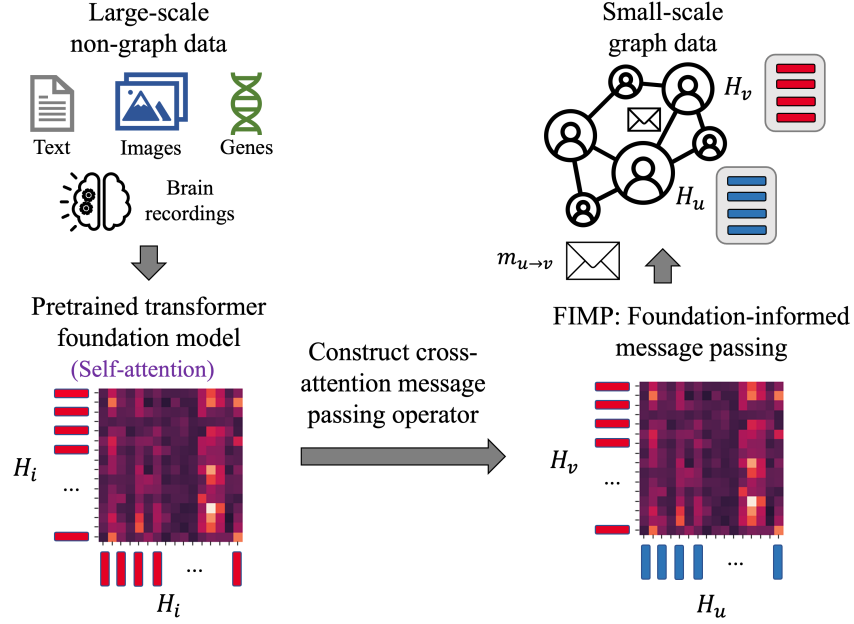


Figure 1: The FIMP framework. FIMP adapts pretrained transformer-based foundational models into message-passing operators.

### 3 Foundation Model-Informed Message Passing

#### 3.1 Preliminaries

We begin by introducing our notation scheme for message-passing GNNs. Let  $\mathcal{G} = (\mathcal{V}, \mathcal{E})$  denote a graph with node features  $x_v \in \mathbb{R}^F$  for each node  $v \in \mathcal{V}$ , where  $F$  is the number of features per node. GNNs iteratively pass messages between neighboring nodes connected by the set of edges  $\mathcal{E}$ , and in the process use both node features and graph structure to learn node representations  $h_v \in \mathbb{R}^D$ , where  $D$  is the hidden dimension of node embeddings. After  $k$  message-passing iterations, node representation  $h_v$  will contain information from its  $k$ -hop neighborhood within the graph. The general update rule for the  $k$ -th layer of a GNN can be represented as follows:

$$h_{\mathcal{N}(v)}^{(k)} = \text{AGGREGATE}^{(k)}(\{h_u^{(k-1)}, u \in \mathcal{N}(v)\}) \quad (1)$$

$$h_v^{(k)} = \text{COMBINE}^{(k)}(h_{\mathcal{N}(v)}^{(k)}, h_v^{(k-1)}), \quad (2)$$

where  $\mathcal{N}(v)$  denotes the neighborhood of node  $v$  and  $h_v^{(k)}$  is the representation of node  $v$  in layer  $k$ . The choice of AGGREGATE and COMBINE vary among different GNN architectures, with the constraint that AGGREGATE should be a permutation-invariant aggregator. A readout function is used to map learned node representations into predictions for feature, node, or graph-level tasks.

#### 3.2 Node tokenization

We define data-specific node tokenization schemes for encoding node features into a sequence of node feature tokens that can be ingested by transformer-based foundation models. Given input node features  $x_v \in \mathbb{R}^F$ , we define a mapping  $\tau : \mathbb{R}^F \rightarrow \mathbb{R}^{F \times D}$  to transform node feature values into a set of feature vectors  $\tau(x_v) = H_v \in \mathbb{R}^{F \times D}$  which will represent the node during the attention message passing step. Note that the embedding process may be task-dependent; for example, time-varying node features may have positional embedding added as part of the embedding process, or language data might have word vectors initialize the feature embedding.

In practice, we utilize positional encoding for timeseries and image datasets, and use a learned embedding table for feature representation in experiments on spatial genomics datasets and citation networks. We note that when adapting pretrained foundation models to downstream graph settings, the encoding scheme used by the foundation model can be

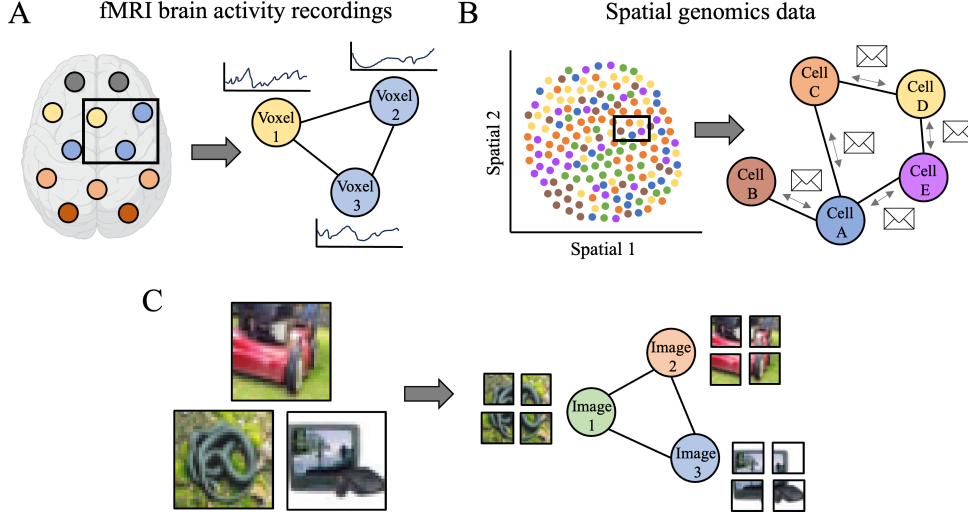


Figure 2: Visualization of graph creation process. (A) For fMRI recordings, the brain is parcellated into 424 regions, which are connected using a K-nearest neighbors graph according to the 3D coordinates of the centroid of each brain region. (B) For spatial genomics data, cells are connected to their nearest neighbors according to 2D coordinates from the original tissue capture. (C) For images, a network is created by probabilistically creating edges between images, with same-class images more likely to be connected.

utilized to tokenize node features if the data is similar. For example, pretrained gene embeddings can be utilized to encode spatial genomics datasets because the gene identities will be similar.

We concatenate the feature information encoding (i.e. positional embedding or learned embedding vector) with a projection of the feature value to obtain the final embedding representing that feature. For the case of positional embedding, this can be represented as:

$$H_v = \tau(x_v) = \text{CONCATENATE}[PE, x_v W_p], \quad (3)$$

where  $PE \in \mathbb{R}^{F \times D}$  represents the positional embedding for the sequence of features for node  $v$ ,  $x_v \in \mathbb{R}^{F \times 1}$  is the input node features, and  $W_p \in \mathbb{R}^{1 \times D}$  represents the projection matrix for feature values. We use sum concatenation to combine feature information and value projection.

### 3.3 Cross-node attention message passing

In order to perform message passing on a tokenized graph, we first define a new cross-attention-based message passing operator between node feature sequences. At a given message passing iteration  $k$ , we perform cross-node multihead attention [14] to create the message that will be passed from source node  $u$  to destination node  $v$ . The context sequence is created from source node  $u$ 's feature sequence  $H_u$ , while the target sequence is formed from destination node  $v$ 's feature vectors  $H_v$ . This can be interpreted as querying the source node for information regarding the destination node in order to create the message. This step can be written as:

$$Q = H_v^{(k-1)} W_q; K = H_u^{(k-1)} W_k; V = H_u^{(k-1)} W_v \quad (4)$$

$$H_{\mathcal{N}(v)}^{(k)} = \text{AGGREGATE}_{u \in \mathcal{N}(v)} \left( \text{softmax} \left( \frac{QK^\top}{\sqrt{D}} \right) V \right) \quad (5)$$

$$H_v^{(k)} = \text{CONCATENATE}[H_v^{(k-1)}, H_{\mathcal{N}(v)}^{(k)}] W_c + b_c, \quad (6)$$

where  $W_q, W_k, W_v$  are weight matrices for query, key, and value vectors,  $H_{\mathcal{N}(v)}^{(k)}$  represents the set of feature vectors obtained from aggregating node  $v$ 's local neighborhood, and  $W_c$  and  $b_c$  represent the weights and biases for the update

function. We note that a deeper multi-layer transformer decoder may be used rather than a simple multihead attention layer to increase expressivity in the message-passing step. Additionally, in practice we compute cross-attention on edges in the graph in batch-wise fashion rather than all at once during the message-passing step to control the computational footprint of message passing. The full FIMP cross-attention message-passing algorithm is summarized in Algorithm 1.

---

**Algorithm 1** FIMP

---

**Require:** Graph  $\mathcal{G} = (\mathcal{V}, \mathcal{E})$ , input features  $h_v^0 \in \mathbb{R}^F$ , feature embedding table  $W_E$

- 1:  $H_v^0 \leftarrow \text{CONCATENATE}[W_E \parallel h_v]$
- 2: **for** node  $v \in N$  **do**
- 3:     **for** node  $u \in \mathcal{N}(v)$  **do**
- 4:          $Q = H_v^{(k-1)} W_q$
- 5:          $K = H_u^{(k-1)} W_k$
- 6:          $V = H_u^{(k-1)} W_v$
- 7:     **end for**
- 8:      $H_{\mathcal{N}(v)}^{(k)} = \text{AGGREGATE} \left( \text{softmax} \left( \frac{QK^\top}{\sqrt{D}} \right) V \right)$
- 9:      $H_v^{(k)} = \text{CONCATENATE}[H_v^{(k-1)}, H_{\mathcal{N}(v)}^{(k)}] W_c + b_c$
- 10: **end for**

---

### 3.4 Foundation-informed message passing

In order to leverage knowledge from pretrained foundation model weights in cross-attention message passing, we replace the multihead cross-attention operation in the base FIMP formulation with the pretrained layer weights of the foundation model. This forms a message creation operator from the foundation model weights, which will learn to construct messages between nodes given their node feature sequences during finetuning. Note that many foundation model layer weights are trained to compute self-attention on single input sequences; in these cases, we adapt the layer definitions for the foundation model weights to perform cross attention between the source and destination weights by constructing the query vectors from the destination node feature sequence, as shown in Equation 4.

## 4 Experiments

### 4.1 Datasets

We test the performance of FIMP on three benchmark tasks: (i) fMRI brain activity signal reconstruction on the UK Biobank (UKB) dataset [26], (ii) gene expression prediction on two spatial transcriptomics datasets, and (iii) masked image reconstruction on a constructed graph of images from the Cifar-100 dataset [13]. The following sections summarize each dataset, and more details are provided in the supplementary.

**UK Biobank dataset** The UK Biobank (UKB) [26] is a large-scale public biomedical database which provides task-based and resting-state functional magnetic resonance imaging (fMRI) recordings from over 40,000 subjects aged 40-69 years old. After standard preprocessing, we take brain activity recordings and divide them into 424 brain regions using the AAL-424 atlas [27], and construct a K-nearest neighbor graph with K=5 based on the 3D coordinates of each brain region.

**Spatial transcriptomics dataset** We benchmark FIMP on two spatial transcriptomics datasets. The Slideseq-V2 spatial transcriptomics dataset [28] is a mouse hippocampal dataset consisting of 41,786 cells and 4,000 genes, with each cell being categorized into one of 14 different cell types. We obtain a second spatial dataset of human heart tissue from the 10X Genomics public spatial data repository, consisting of 4247 cells expressed and 36601 genes. For both datasets, we follow standard preprocessing and normalization procedures for RNA sequencing data.

**Cifar-100** The Cifar-100 image dataset [13] consists of 60,000 32x32 pixel images belonging to 100 classes. We construct an image graph from Cifar-100, where each node represents an entire original image in the dataset, by connecting images to other images of the same or different class with some probability. The resulting graph contains nodes with connections to other image nodes of the same and different class, creating a challenging node-image reconstruction task given the high-dimensional features of an image and the semantic information present in images.

Table 1: Benchmark on UK Biobank fMRI recording reconstruction. Performance is reported across 5 runs in terms of Mean Squared Error (MSE) and  $R^2$ . FIMP improves upon baselines by 25.8%, with a further improvement of 2.8% by adapting a foundation model for brain activity as the message-passing operator.

Method	Masking Strategy	MSE ( $\downarrow$ )	$R^2$ ( $\uparrow$ )
GCN	Replace noise	$0.554 \pm 0.00002$	$0.189 \pm 0.00003$
	Fill in mean	$0.513 \pm 0.00019$	$0.248 \pm 0.00028$
	Linear interpolation	$0.535 \pm 0.00137$	$0.217 \pm 0.00200$
GraphSAGE	Replace noise	$0.534 \pm 0.00107$	$0.218 \pm 0.00157$
	Fill in mean	$0.464 \pm 0.00039$	$0.320 \pm 0.00057$
	Linear interpolation	$0.500 \pm 0.00094$	$0.268 \pm 0.00138$
GAT	Replace noise	$0.548 \pm 0.00004$	$0.197 \pm 0.00007$
	Fill in mean	$0.505 \pm 0.00005$	$0.260 \pm 0.00007$
	Linear interpolation	$0.527 \pm 0.00052$	$0.229 \pm 0.00076$
GIN	Replace noise	$0.564 \pm 0.00131$	$0.174 \pm 0.00192$
	Fill in mean	$0.533 \pm 0.00185$	$0.220 \pm 0.00271$
	Linear interpolation	$0.559 \pm 0.00061$	$0.181 \pm 0.00090$
GraphMAE	Replace noise	$0.582 \pm 0.00070$	$0.147 \pm 0.00103$
	Fill in mean	$0.544 \pm 0.00030$	$0.203 \pm 0.00044$
	Linear interpolation	$0.573 \pm 0.00091$	$0.160 \pm 0.00134$
GPS Graph Transformer	Replace noise	$0.577 \pm 0.00279$	$0.154 \pm 0.00408$
	Fill in mean	$0.547 \pm 0.01030$	$0.198 \pm 0.01506$
	Linear interpolation	$0.557 \pm 0.01034$	$0.184 \pm 0.01512$
FIMP	Tokenization + PE	$0.288 \pm 0.00713$	$0.578 \pm 0.01043$
FIMP + BrainLM	Tokenization + PE	<b><math>0.267 \pm 0.00493</math></b>	<b><math>0.606 \pm 0.00972</math></b>

## 4.2 Baseline Methods

We compare FIMP against a set of popular message-passing architectures, including GCN [29], GraphSAGE [30], GAT[31], and GIN [32] on self-supervised reconstruction tasks. We also compare against GraphMAE [33], a recent graph autoencoder technique which utilizes masked learning objectives, as well as GPS Graph Transformer, a SOTA graph transformer architecture [23].

## 4.3 Experimental Setup

For all experiment datasets, we perform a random nodewise split on the graph dataset to form training, validation, and test splits. To prevent out-of-memory (OOM) errors on large graph datasets (e.g. large spatial datasets), we utilize the GraphSAINT subgraph sampler [34] to minibatch across the entire graph for all experiments. All GNN models are implemented with two message-passing layers, with an equal trainable parameter budget for each experiment to ensure similar learning capacity. We conduct a grid search to find the optimal learning rate, dropout rate, and weight decay for each architecture, which are summarized in the Appendix A.7. All models use the Adam optimizer with default parameters, with a cosine annealing learning rate scheduler with 5 annealing cycles throughout training. All experiments and models were implemented using Pytorch Geometric Python library [35].

In the fMRI recording reconstruction, we construct a KNN graph using the 3D coordinates of each brain region. We tokenize the signal value of each voxel in the recording into patches of 20 timepoints, and train FIMP to reconstruct 50% of the tokens per voxel. For baseline architectures, we provide the 400 timepoint series as an input vector with masked patches filled in by (i) replacing with random noise, (ii) replacing with the mean value, and (iii) interpolating between adjacent unmasked points.

For masked gene expression tasks, we learn an embedding table with a unique vector for each gene in the dataset which will be used in node tokenization. In experiments involving pretrained foundation models, the embedding table is initialized from pretrained embedding weights of the foundation model, and is further trained during finetuning. We sample a fixed number of nonzero genes per cell with replacement as input, and embed each gene using its learned embedding vector concatenated with a projection of its expression value in that cell. In practice, we sample 50 and 30 nonzero genes with replacement for the mouse hippocampus [28] and human heart datasets respectively, and use a

Table 2: Experimental results on masked gene expression prediction on the human heart and mouse hippocampus spatial genomics datasets. Performance is reported across 5 runs in terms of MSE and  $R^2$ . FIMP outperforms baseline methods on predicting masked gene expression values on both datasets in both full and limited data settings.

Data size	Method	Mouse Hippocampus		Human Heart	
		MSE ( $\downarrow$ )	$R^2$ ( $\uparrow$ )	MSE ( $\downarrow$ )	$R^2$ ( $\uparrow$ )
Full	GCN	0.0178 $\pm$ 0.00056	0.264 $\pm$ 0.00930	0.0015 $\pm$ 0.00005	0.776 $\pm$ 0.01481
	GraphSAGE	0.0144 $\pm$ 0.00038	0.387 $\pm$ 0.02043	0.0016 $\pm$ 0.00012	0.778 $\pm$ 0.01537
	GAT	0.0185 $\pm$ 0.00120	0.237 $\pm$ 0.02509	0.0015 $\pm$ 0.00006	0.770 $\pm$ 0.01759
	GIN	0.0166 $\pm$ 0.00084	0.297 $\pm$ 0.02919	0.0015 $\pm$ 0.00012	0.759 $\pm$ 0.01577
	GraphMAE	0.0178 $\pm$ 0.00044	0.271 $\pm$ 0.02661	0.0015 $\pm$ 0.00014	0.762 $\pm$ 0.00568
	GPS	0.0139 $\pm$ 0.00077	0.416 $\pm$ 0.02658	0.0015 $\pm$ 0.00010	0.764 $\pm$ 0.01738
	FIMP (ours)	0.0096 $\pm$ 0.00077	0.562 $\pm$ 0.03197	0.0011 $\pm$ 0.00005	0.832 $\pm$ 0.01032
	FIMP + GenePT (ours)	<b>0.0094 <math>\pm</math> 0.00060</b>	<b>0.602 <math>\pm</math> 0.02590</b>	<b>0.0010 <math>\pm</math> 0.00005</b>	<b>0.837 <math>\pm</math> 0.02170</b>
Limited	GCN	0.0211 $\pm$ 0.0018	0.0236 $\pm$ 0.0457	0.0045 $\pm$ 0.00019	0.3368 $\pm$ 0.04453
	GraphSAGE	0.0181 $\pm$ 0.0012	0.1853 $\pm$ 0.0306	0.0054 $\pm$ 0.00033	0.2080 $\pm$ 0.01973
	GAT	0.0201 $\pm$ 0.0008	0.0905 $\pm$ 0.0233	0.0043 $\pm$ 0.00023	0.3468 $\pm$ 0.02313
	GIN	0.0175 $\pm$ 0.0009	0.1707 $\pm$ 0.0424	0.0025 $\pm$ 0.00029	0.6625 $\pm$ 0.01269
	GraphMAE	0.0178 $\pm$ 0.0006	0.1538 $\pm$ 0.0254	0.0024 $\pm$ 0.00016	0.6589 $\pm$ 0.01715
	GPS	0.0149 $\pm$ 0.0012	0.2977 $\pm$ 0.0308	0.0024 $\pm$ 0.00031	0.6538 $\pm$ 0.01043
	FIMP (ours)	0.0134 $\pm$ 0.0009	0.3815 $\pm$ 0.0226	0.0021 $\pm$ 0.00003	0.6955 $\pm$ 0.02048
	FIMP + ViT (ours)	0.0128 $\pm$ 0.0010	0.3506 $\pm$ 0.0452	0.0042 $\pm$ 0.00089	0.4026 $\pm$ 0.08102
	FIMP + GenePT (ours)	0.0129 $\pm$ 0.0005	0.4058 $\pm$ 0.0302	0.0013 $\pm$ 0.00023	0.7952 $\pm$ 0.01430
	FIMP + scGPT (ours)	<b>0.0119 <math>\pm</math> 0.0008</b>	<b>0.4612 <math>\pm</math> 0.0029</b>	<b>0.0011 <math>\pm</math> 0.00008</b>	<b>0.8119 <math>\pm</math> 0.01428</b>

masking ratio of 20 percent for both datasets for the full data setting. In the limited data setting, we make the task more challenging by increasing the masking rate to 80 percent and limiting the number of cells in the dataset to 1000 cells.

On the masked image reconstruction task, we follow the same masking procedure and positional encoding scheme as the Masked Autoencoder [36]. We use a 2-layer FIMP encoder and an additional FIMP layer as the decoder for the framework, and follow the convention of applying the encoder layer to only unmasked patches within each image. For each image, we use a patch size of 4x4 pixels with a masking rate of 20% on each image. All models are trained to directly reconstruct pixel values of the masked patches in the input image.

#### 4.4 Results

The results of our benchmarking on fMRI brain activity and spatial genomics datasets are summarized in Tables 1 and 2, respectively.

For the fMRI recording reconstruction task, we report performance of baseline GNN architectures using different methods for masking out signal time windows, including filling in the mean value, replacing with noise, and linearly interpolating between adjacent timepoints. FIMP improves on the nearest baseline by 25% at fMRI brain activity reconstruction, outperforming strong masked prediction graph autoencoder and graph transformer baselines. We note that this performance improvement comes at an equivalent parameter budget for FIMP compared to other GNNs. We attribute this strong performance to the node tokenization scheme, which is designed efficiently to tokenize fMRI recordings while incorporating positional encoding for the time-varying signals. Adapting a foundational fMRI brain activity model, BrainLM [11], further improves performance by 3%, demonstrating improved performance from adapting a pretrained model of brain activity as the message passing operator in FIMP.

In our second task, we report mean square error (MSE) and  $R^2$  of masked gene expression reconstruction on both spatial tissue datasets in a full data setting as well as a limited data setting, where the number of training nodes is severely restricted to only contain a few training nodes for supervision in each input subgraph (Table 2). FIMP again outperforms baseline methods at reconstructing gene expression values on both datasets, demonstrating that the learned gene embedding allows FIMP to encode genes more effectively compared to baseline GNNs. We also note a substantial increase in performance in the limited data setting when pretrained single-cell foundation model weights are adapted as message passing operators on the spatial tissues. First, we examine initializing the gene embedding table in FIMP using gene embeddings obtained by summarizing NCBI gene summaries using GPT-3.5, as described in GenePT [37]. We observe a 2.4% and 10% increase in reconstruction  $R^2$  on the mouse hippocampus and human heart tissues respectively compared to the baseline FIMP model. We next adapt both the pretrained gene embedding and layer weights from

scGPT [9], a SOTA single-cell foundation model, into a message passing operator using FIMP, and observe another 5.5% and 1.7% improvement in performance. We hypothesize that the pretrained foundation model weights are especially beneficial in limited and rare data settings, where the model can leverage its more general knowledge from non-graph pretraining. Notably, adapting a pretrained Vision Transformer model [38] into a message-passing operator did not result in the same performance improvement as using a pretrained single-cell foundational model, despite having more trainable parameters overall. This demonstrates that the performance improvement stems from the foundation model having been pretraining on similar single-cell data, resulting in a positive transfer to downstream graph tasks.

Table 3: Masked image reconstruction results on Cifar-100. Performance is measured in terms of MSE and R2 for masked image reconstruction.

Method	Cifar-100	
	MSE ( $\downarrow$ )	$R^2$ ( $\uparrow$ )
GCN	$0.673 \pm 0.003$	$0.333 \pm 0.006$
GraphSAGE	$0.473 \pm 0.003$	$0.526 \pm 0.008$
GAT	$0.668 \pm 0.016$	$0.331 \pm 0.018$
GraphMAE	$0.753 \pm 0.010$	$0.247 \pm 0.002$
FIMP	<b><math>0.306 \pm 0.010</math></b>	<b><math>0.696 \pm 0.008</math></b>

For our third task, we evaluate FIMP’s ability to effectively tokenize entire images per node and perform reconstruction of masked patches in Table 3. FIMP performs 17% better than the closest baseline method in terms of  $R^2$  at reconstructing masked pixel values in Cifar-100 images. This further demonstrates the viability of FIMP on diverse data domains with rich node information available. We hypothesize that the tokenization approach, which closely follows standard tokenization procedures in Computer Vision, allows FIMP to encode images more effectively in patches and perform reconstruction. Additionally, 2D positional embedding gives FIMP more information about the relative position of different image patches compared to conventional GNN approaches. We believe that this is a promising approach for learning on larger-resolution image networks.

## 5 Conclusion

In this work, we introduce the Foundation-Informed Message Passing (FIMP) framework, a novel framework which serves as a bridge between foundation models and Graph Neural Networks (GNNs). Our approach involves constructing message-passing operators using pretrained foundation model weights, ultimately enhancing the performance of graph-based tasks across various data domains. The FIMP framework offers a promising solution for leveraging the versatility and adaptability of foundation models in graph-structured settings, potentially opening up new avenues for applications in Deep Learning.

There are several avenues for improvement upon the FIMP operator, which can be addressed in future work. A more efficient selection strategy for node features in sparse datasets such as those seen in spatial genomics might yield better node representations during training. Additionally, sparse or linear attention mechanisms can be implemented to improve the efficiency and overhead of the architecture, especially considering the size of foundation model weights. Finally, incorporating edge features, or possibly features assigned to the relationship between specific node features, may also be an interesting direction for further contextualizing feature-level interactions in graph-structured data.

## References

- [1] Rishi Bommasani, Drew A Hudson, Ehsan Adeli, Russ Altman, Simran Arora, Sydney von Arx, Michael S Bernstein, Jeannette Bohg, Antoine Bosselut, Emma Brunskill, et al. On the opportunities and risks of foundation models. *arXiv preprint arXiv:2108.07258*, 2021.
- [2] Alec Radford, Karthik Narasimhan, Tim Salimans, Ilya Sutskever, et al. Improving language understanding by generative pre-training. 2018.
- [3] Jacob Devlin, Ming-Wei Chang, Kenton Lee, and Kristina Toutanova. Bert: Pre-training of deep bidirectional transformers for language understanding. *arXiv preprint arXiv:1810.04805*, 2018.
- [4] Yen-Chun Chen, Linjie Li, Licheng Yu, Ahmed El Kholy, Faisal Ahmed, Zhe Gan, Yu Cheng, and Jingjing Liu. Uniter: Universal image-text representation learning. In *European conference on computer vision*, pages 104–120. Springer, 2020.



- [5] Tom Brown, Benjamin Mann, Nick Ryder, Melanie Subbiah, Jared D Kaplan, Prafulla Dhariwal, Arvind Nee-lakantan, Pranav Shyam, Girish Sastry, Amanda Askell, et al. Language models are few-shot learners. *Advances in neural information processing systems*, 33:1877–1901, 2020.
- [6] Alec Radford, Jong Wook Kim, Chris Hallacy, Aditya Ramesh, Gabriel Goh, Sandhini Agarwal, Girish Sastry, Amanda Askell, Pamela Mishkin, Jack Clark, et al. Learning transferable visual models from natural language supervision. In *International conference on machine learning*, pages 8748–8763. PMLR, 2021.
- [7] Lu Yuan, Dongdong Chen, Yi-Ling Chen, Noel Codella, Xiyang Dai, Jianfeng Gao, Houdong Hu, Xuedong Huang, Boxin Li, Chunyuan Li, et al. Florence: A new foundation model for computer vision. *arXiv preprint arXiv:2111.11432*, 2021.
- [8] Suchin Gururangan, Ana Marasović, Swabha Swayamdipta, Kyle Lo, Iz Beltagy, Doug Downey, and Noah A Smith. Don’t stop pretraining: Adapt language models to domains and tasks. *arXiv preprint arXiv:2004.10964*, 2020.
- [9] Haotian Cui, Chloe Wang, Hassaan Maan, Kuan Pang, Fengning Luo, and Bo Wang. scgpt: towards building a foundation model for single-cell multi-omics using generative ai. *bioRxiv*, pages 2023–04, 2023.
- [10] Christina V Theodoris, Ling Xiao, Anant Chopra, Mark D Chaffin, Zeina R Al Sayed, Matthew C Hill, Helene Mantineo, Elizabeth M Brydon, Zexian Zeng, X Shirley Liu, et al. Transfer learning enables predictions in network biology. *Nature*, pages 1–9, 2023.
- [11] Josue Ortega Caro, Antonio Henrique Oliveira Fonseca, Christopher Averill, Syed A Rizvi, Matteo Rosati, James L Cross, Prateek Mittal, Emanuele Zappala, Daniel Levine, Rahul M Dhodapkar, et al. Brainlm: A foundation model for brain activity recordings. *bioRxiv*, pages 2023–09, 2023.
- [12] Jiawei Liu, Cheng Yang, Zhiyuan Lu, Junze Chen, Yibo Li, Mengmei Zhang, Ting Bai, Yuan Fang, Lichao Sun, Philip S Yu, et al. Towards graph foundation models: A survey and beyond. *arXiv preprint arXiv:2310.11829*, 2023.
- [13] Alex Krizhevsky, Geoffrey Hinton, et al. Learning multiple layers of features from tiny images. 2009.
- [14] Ashish Vaswani, Noam Shazeer, Niki Parmar, Jakob Uszkoreit, Llion Jones, Aidan N Gomez, Łukasz Kaiser, and Illia Polosukhin. Attention is all you need. *Advances in neural information processing systems*, 30, 2017.
- [15] Alec Radford, Jeffrey Wu, Rewon Child, David Luan, Dario Amodei, Ilya Sutskever, et al. Language models are unsupervised multitask learners. *OpenAI blog*, 1(8):9, 2019.
- [16] Hugo Touvron, Louis Martin, Kevin Stone, Peter Albert, Amjad Almahairi, Yasmine Babaei, Nikolay Bashlykov, Soumya Batra, Prajwal Bhargava, Shruti Bhosale, et al. Llama 2: Open foundation and fine-tuned chat models. *arXiv preprint arXiv:2307.09288*, 2023.
- [17] Mathilde Caron, Hugo Touvron, Ishan Misra, Hervé Jégou, Julien Mairal, Piotr Bojanowski, and Armand Joulin. Emerging properties in self-supervised vision transformers. In *Proceedings of the IEEE/CVF international conference on computer vision*, pages 9650–9660, 2021.
- [18] Kaiming He, Haoqi Fan, Yuxin Wu, Saining Xie, and Ross Girshick. Momentum contrast for unsupervised visual representation learning. In *Proceedings of the IEEE/CVF conference on computer vision and pattern recognition*, pages 9729–9738, 2020.
- [19] Ze Liu, Yutong Lin, Yue Cao, Han Hu, Yixuan Wei, Zheng Zhang, Stephen Lin, and Baining Guo. Swin transformer: Hierarchical vision transformer using shifted windows. In *Proceedings of the IEEE/CVF international conference on computer vision*, pages 10012–10022, 2021.
- [20] Yuning You, Tianlong Chen, Yongduo Sui, Ting Chen, Zhangyang Wang, and Yang Shen. Graph contrastive learning with augmentations. *Advances in neural information processing systems*, 33:5812–5823, 2020.
- [21] Yanqiao Zhu, Yichen Xu, Feng Yu, Qiang Liu, Shu Wu, and Liang Wang. Deep graph contrastive representation learning. *arXiv preprint arXiv:2006.04131*, 2020.
- [22] Petar Velickovic, William Fedus, William L Hamilton, Pietro Liò, Yoshua Bengio, and R Devon Hjelm. Deep graph infomax. *ICLR (Poster)*, 2(3):4, 2019.
- [23] Ladislav Rampášek, Michael Galkin, Vijay Prakash Dwivedi, Anh Tuan Luu, Guy Wolf, and Dominique Beaini. Recipe for a general, powerful, scalable graph transformer. *Advances in Neural Information Processing Systems*, 35:14501–14515, 2022.
- [24] Jiayan Guo, Lun Du, and Hengyu Liu. Gpt4graph: Can large language models understand graph structured data? an empirical evaluation and benchmarking. *arXiv preprint arXiv:2305.15066*, 2023.
- [25] Heng Wang, Shangbin Feng, Tianxing He, Zhaoxuan Tan, Xiaochuang Han, and Yulia Tsvetkov. Can language models solve graph problems in natural language? *arXiv preprint arXiv:2305.10037*, 2023.

- [26] Karla L Miller, Fidel Alfaro-Almagro, Neal K Bangerter, David L Thomas, Essa Yacoub, Junqian Xu, Andreas J Bartsch, Saad Jbabdi, Stamatios N Sotiropoulos, Jesper LR Andersson, et al. Multimodal population brain imaging in the uk biobank prospective epidemiological study. *Nature neuroscience*, 19(11):1523–1536, 2016.
- [27] Samaneh Nemati, Teddy J Akiki, Jeremy Roscoe, Yumeng Ju, Christopher L Averill, Samar Fouda, Arpan Dutta, Shane McKie, John H Krystal, JF William Deakin, et al. A unique brain connectome fingerprint predates and predicts response to antidepressants. *iScience*, 23(1), 2020.
- [28] Robert R Stickels, Evan Murray, Pawan Kumar, Jilong Li, Jamie L Marshall, Daniela J Di Bella, Paola Arlotta, Evan Z Macosko, and Fei Chen. Highly sensitive spatial transcriptomics at near-cellular resolution with slide-seq2. *Nature biotechnology*, 39(3):313–319, 2021.
- [29] Thomas N Kipf and Max Welling. Semi-supervised classification with graph convolutional networks. *arXiv preprint arXiv:1609.02907*, 2016.
- [30] Will Hamilton, Zhitao Ying, and Jure Leskovec. Inductive representation learning on large graphs. *Advances in neural information processing systems*, 30, 2017.
- [31] Petar Veličković, Guillem Cucurull, Arantxa Casanova, Adriana Romero, Pietro Lio, and Yoshua Bengio. Graph attention networks. *arXiv preprint arXiv:1710.10903*, 2017.
- [32] Keyulu Xu, Weihua Hu, Jure Leskovec, and Stefanie Jegelka. How powerful are graph neural networks? *arXiv preprint arXiv:1810.00826*, 2018.
- [33] Zhenyu Hou, Xiao Liu, Yukuo Cen, Yuxiao Dong, Hongxia Yang, Chunjie Wang, and Jie Tang. Graphmae: Self-supervised masked graph autoencoders. In *Proceedings of the 28th ACM SIGKDD Conference on Knowledge Discovery and Data Mining*, pages 594–604, 2022.
- [34] Hanqing Zeng, Hongkuan Zhou, Ajitesh Srivastava, Rajgopal Kannan, and Viktor Prasanna. Graphsaint: Graph sampling based inductive learning method. *arXiv preprint arXiv:1907.04931*, 2019.
- [35] Matthias Fey and Jan Eric Lenssen. Fast graph representation learning with pytorch geometric. *arXiv preprint arXiv:1903.02428*, 2019.
- [36] Kaiming He, Xinlei Chen, Saining Xie, Yanghao Li, Piotr Dollár, and Ross Girshick. Masked autoencoders are scalable vision learners. In *Proceedings of the IEEE/CVF conference on computer vision and pattern recognition*, pages 16000–16009, 2022.
- [37] Yiqun T Chen and James Zou. Genept: A simple but hard-to-beat foundation model for genes and cells built from chatgpt. *bioRxiv*, pages 2023–10, 2023.
- [38] Alexey Dosovitskiy, Lucas Beyer, Alexander Kolesnikov, Dirk Weissenborn, Xiaohua Zhai, Thomas Unterthiner, Mostafa Dehghani, Matthias Minderer, Georg Heigold, Sylvain Gelly, et al. An image is worth 16x16 words: Transformers for image recognition at scale. *arXiv preprint arXiv:2010.11929*, 2020.
- [39] Gholamreza Salimi-Khorshidi, Gwenaëlle Douaud, Christian F Beckmann, Matthew F Glasser, Ludovica Griffanti, and Stephen M Smith. Automatic denoising of functional mri data: combining independent component analysis and hierarchical fusion of classifiers. *Neuroimage*, 90:449–468, 2014.
- [40] Chadi G Abdallah. Brain networks associated with covid-19 risk: Data from 3662 participants. *Chronic Stress*, 5:24705470211066770, 2021.
- [41] Giovanni Palla, Hannah Spitzer, Michal Klein, David Fischer, Anna Christina Schaar, Louis Benedikt Kuemmerle, Sergei Rybakov, Ignacio L Ibarra, Olle Holmberg, Isaac Virshup, et al. Squidpy: a scalable framework for spatial omics analysis. *Nature methods*, 19(2):171–178, 2022.
- [42] Prithviraj Sen, Galileo Namata, Mustafa Bilgic, Lise Getoor, Brian Galligher, and Tina Eliassi-Rad. Collective classification in network data. *AI magazine*, 29(3):93–93, 2008.
- [43] Oleksandr Shchur, Maximilian Mumme, Aleksandar Bojchevski, and Stephan Günnemann. Pitfalls of graph neural network evaluation. *arXiv preprint arXiv:1811.05868*, 2018.
- [44] Shantanu Thakoor, Corentin Tallec, Mohammad Gheshlaghi Azar, Mehdi Azabou, Eva L Dyer, Remi Munos, Petar Veličković, and Michal Valko. Large-scale representation learning on graphs via bootstrapping. *arXiv preprint arXiv:2102.06514*, 2021.
- [45] Aditya Grover and Jure Leskovec. node2vec: Scalable feature learning for networks. In *Proceedings of the 22nd ACM SIGKDD international conference on Knowledge discovery and data mining*, pages 855–864, 2016.
- [46] Shizhen Yan, Juntao Chen, Xiaojuan Yin, Ziliang Zhu, Ziping Liang, Hua Jin, Han Li, Jianzhong Yin, Yunpeng Jiang, and Yaoyuan Xia. The structural basis of age-related decline in global motion perception at fast and slow speeds. *Neuropsychologia*, 183:108507, 2023.

- [47] Breanne E Kearney and Ruth A Lanius. The brain-body disconnect: A somatic sensory basis for trauma-related disorders. *Frontiers in Neuroscience*, 16:1881, 2022.
- [48] Saurabh Dey, Soumya Basu, and Amit Ranjan. Revisiting the role of cd63 as pro-tumorigenic or anti-tumorigenic tetraspanin in cancers and its theragnostic implications. *Advanced Biology*, page 2300078, 2023.
- [49] Charlotte Aaberg-Jessen, Mia D Sørensen, Ana LSA Matos, José M Moreira, Nils Brünner, Arnon Knudsen, and Bjarne W Kristensen. Co-expression of timp-1 and its cell surface binding partner cd63 in glioblastomas. *BMC cancer*, 18:1–16, 2018.
- [50] Kuansan Wang, Zhihong Shen, Chiyuan Huang, Chieh-Han Wu, Yuxiao Dong, and Anshul Kanakia. Microsoft academic graph: When experts are not enough. *Quantitative Science Studies*, 1(1):396–413, 2020.

## A Appendix

### A.1 Dataset Details

We first evaluate the performance of FIMP in self-supervised reconstruction of fMRI recordings from the publicly-available UK Biobank (UKB) [26] dataset. The UKB provides task-based and resting-state functional magnetic resonance imaging (fMRI) recordings along with medical records from over 40,000 subjects aged 40-69 years old. We take all 76250 brain activity recordings from UKB and use a 80/10/10 split for training, validation, and test respectively. Standard preprocessing was done on all recordings, including motion correction, normalization, temporal filtering, and ICA denoising [39, 40]. We used a parcellation of the brain into 424 brain regions using the AAL-424 atlas [27], and normalized the recordings per voxel by subtracting the mean of each voxel and scaling by the standard deviation of signal values from all 1000 recordings.

Next, we evaluate FIMP on a masked gene expression prediction task on two spatial transcriptomics datasets. The Slideseq-V2 spatial transcriptomics dataset [28] is a mouse hippocampal dataset with high RNA capture efficiency and near-cellular spatial resolution. The data consists of 41,786 cells, expressed in 4,000 genes, with each cell being categorized into one of 14 different cell types. We obtain the dataset from the Squidpy library [41], and follow standard preprocessing and normalization procedures, including normalizing expression values roughly between 0 and 1 by scaling with the 99th percentile of the data. We also benchmark on a 10X Genomics spatial transcriptomics dataset consisting of human heart tissue following the same normalization procedure.

We also evaluate FIMP’s ability to do masked image reconstruction on an image network dataset constructed from the Cifar-100 image dataset, which contains 60k images belonging to 100 classes [13]. We split the Cifar-100 dataset into 40k/10k/10k train/val/test image splits, and connect training set images to each other with 2% probability for same-class images, and 0.01% probability for images of different classes. This yields a training graph with an average node degree of 12, with most image neighbors belonging to the same class. We create separate image graphs for the validation and test sets, and adjust probabilities to maintain the average node degree of 12.

Finally, we benchmark FIMP on several standard benchmark datasets for unsupervised node classification. The Cora dataset [42] consists of 2,708 nodes each comprising a scientific paper, with 5,429 edges representing citation links, 7 classes, and 1,433 features per node. Pubmed [42] similarly contains 19,717 nodes, 44,338 edges, 3 classes, and 500 node features. Amazon Computers [43] is a segment of the Amazon co-purchase graph, with 13,381 nodes representing goods and edges denoting items frequently bought together.

### A.2 Experiments Setup Details

For fMRI recording reconstruction, we construct a graph of brain regions, by connecting each region to its 5 nearest neighbors based on the xyz coordinates. We implement feature embedding for FIMP by tokenizing 400 timepoints of signal per brain region into 20 patches of 20 timepoints, with positional encoding optionally added. We mask 50% of the tokens per voxel and train FIMP to reconstruct the missing signal tokens. For baseline architectures which represent nodes as a single vector, we provide the 400 timepoint series as an input vector, and benchmark against three options for masking timepoint patches: (i) replacing masked signal patches with random noise, (ii) replacing values with the mean signal value, and (iii) interpolating between adjacent visible signal values around the masked timepoint patch.

For masked gene expression tasks, many genes are zero expressed and do not convey information about the state of a cell. We therefore sample a fixed number of nonzero expressed genes per cell with replacement, and encode these to represent a cell in FIMP. For baseline architectures, the data is given as a vector input for each cell, with the length of the vector corresponding to the total number of genes in the dataset. Note that FIMP’s representation of the expression data is more flexible, since the number of genes in the dataset does not determine the input size of data in FIMP. In practice, we sample 50 and 30 nonzero genes with replacement for the mouse hippocampus [28] and human heart datasets respectively, and use a masking ratio of 20 percent for both datasets.

### A.3 Supplementary Results

We provide benchmarks on standard datasets for unsupervised node classification against recent contrastive graph-based architectures including DGI [22], GRACE [21], and BGRL [44] in addition to GraphMAE. We include the random initialization baseline from [22], which uses a randomly initialized GCN encoder to encode nodes in order to measure the quality of inductive biases in the encoder model. Baseline methods were implemented using publicly available code whenever possible. The performance of a linear classifier on raw node features and node2vec [45] embeddings is included as baselines for performance attainable from node features and graph structure alone, respectively.

Table 4: Experimental results on node classification. For self-supervised methods, models are pretrained using a feature reconstruction objective, and test set accuracy of a linear classifier is reported based on learned node representations. The available data for each training method is shown in the second column, where **X** and **A** denote node features and graph adjacency information, respectively.

Method	Available Data	Cora	Pubmed	Amazon Computers
Raw Features	<b>X</b>	47.3 $\pm$ 2.27	63.7 $\pm$ 3.13	85.7 $\pm$ 1.12
DeepWalk	<b>A</b>	70.1 $\pm$ 1.42	64.5 $\pm$ 1.97	86.3 $\pm$ 0.95
Random-init	<b>X, A</b>	70.2 $\pm$ 1.20	66.3 $\pm$ 3.83	84.7 $\pm$ 0.79
DGI	<b>X, A</b>	69.6 $\pm$ 2.36	68.2 $\pm$ 4.14	83.9 $\pm$ 1.34
GRACE	<b>X, A</b>	<b>80.3 <math>\pm</math> 1.99</b>	76.0 $\pm$ 4.10	81.4 $\pm$ 0.63
BGRL	<b>X, A</b>	79.7 $\pm$ 1.69	73.4 $\pm$ 3.71	<b>84.9 <math>\pm</math> 1.03</b>
GraphMAE	<b>X, A</b>	78.7 $\pm$ 2.02	73.8 $\pm$ 1.86	74.9 $\pm$ 1.75
FIMP (masking)	<b>X, A</b>	73.0 $\pm$ 3.10	<b>76.2 <math>\pm</math> 0.88</b>	77.8 $\pm$ 2.07

For all unsupervised node classification experiments, we follow the linear classifier evaluation scheme from [22], where models are first trained in unsupervised fashion to learn node representations. Then, nodes are encoded, and a  $\mathcal{L}_2$ -normalized linear classifier is fitted on the node embeddings to measure the quality of learned node representations. We repeat training for 5 runs, and report averaged performance on each dataset. Due to the sparsity of BoW node features, we sample nonzero features with replacement for feature embedding on the forward pass through FIMP, rather than embedding all features. This saves computations, and represents nodes with their present features as they participate in cross-attention within FIMP. Wherever possible, we follow the specified parameters for each architecture on each dataset if reported in their respective training procedure. All training experiments are done on an NVIDIA rtx5000 GPU with 16GB of memory. To ensure that all methods fit within memory constraints, we perform subgraph sampling using GraphSAINT random walk-based sampler [34] to avoid computing message-passing over the entire graph at once.

Table 4 summarizes the results for unsupervised node classification. We find that FIMP performs on par with strong self-supervised approaches on benchmark datasets where nodes consist of bag-of-words features. We note that on these datasets, there is no explicit additional information to be encoded for each individual feature, and the task therefore does not take advantage of FIMP’s expressiveness in representing individual node features. We believe that FIMP is more well-suited for tasks where rich information can be encoded per node and node feature. FIMP’s comparable performance on standard datasets, however, suggests that it may be used in conjunction with other GNN layers in more complex architectures in order to introduce interpretability and more expressive feature encoding.

#### A.4 Attention Case Study 1: Functional Region Attention in fMRI Recordings Networks

During message passing on the fMRI recording-constructed graph, FIMP generates cross-attention matrices between brain voxels and their 5 closest neighbors in the K-neighbor graph. We group the 424 brain voxels into 7 functional regions, namely the visual, sensorimotor, ventral salience, dorsal salience, central executive, default mode, and subcortical regions of the brain. Taking 100 unseen test set recordings, we extract attention matrices between all connected nodes, average the attention matrices across timepoints per node, and split patient recordings according to conditions such as Age and post-traumatic stress disorder (PTSD) score. We then average attention values across patient recordings with the same condition, and aggregate the node attention into the 7 functional regions, allowing us to examine differences in functional region attention between patients with different conditions.

In Figure 3A, the attention between functional regions is shown between patients below 65 years of age (left) and those above 65 (middle). The difference in attention between the two groups, as visualized on the rightmost plot, indicates that older patients tend to have higher attention between the dorsal salience regions and visual cortex regions. This follows previous literature that shows changes in dorsal pathways as people age [46]. Furthermore, Figure 3B shows similar visualizations for patients with high and low PTSD scores, revealing higher attention between sensorimotor areas and central executive, and subcortical areas. This also follows previous literature on the somatosensory basis of PTSD, where arousal and higher-order capacities get affected [47]. These patterns in attention reveal potential differences in functional region attention picked up by FIMP among patients of varying conditions during unsupervised training on fMRI recordings.

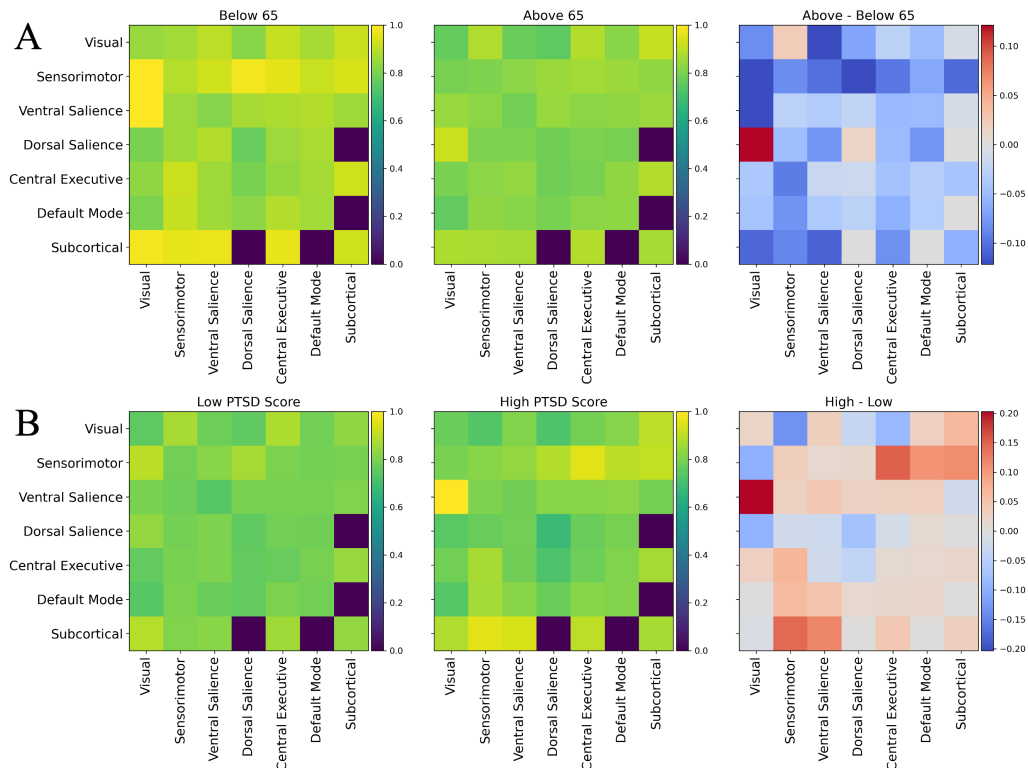


Figure 3: Visualizations of FIMP feature-level attention between different functional groups in the brain. (A) Averaged attention heatmaps between functional regions of the brain for different age populations, with the difference in attention by age group visualized on the right subplot. (B) Similar heatmaps visualized for post-traumatic stress disorder (PTSD) scores, highlighting differences in attention in patients with low vs high PTSD score.

### A.5 Attention Case Study 2: Gene Interactions in Spatial Transcriptomics

In spatial genomics datasets, each node corresponds to a cell which is represented by a set of expressed genes. During message-passing FIMP provides attention matrices representing interactions between genes of different cells. Gene interactions receiving higher attention between nodes can highlight possible biological connections which can be avenues of potential further exploration in the data. For example, Figure 4A shows an averaged attention heatmap across all self-edges connecting astrocyte cells in a subgraph sampled from the mouse hippocampus dataset [28]. This astrocyte-astrocyte feature-level attention matrix identifies a key interaction between CD63, a member of the tetraspanin family of cell surface proteins, and CKAP2L, a mitotic spindle protein controlling cellular division. Previous work has identified that CD63 may be either pro- or anti-tumorigenic, depending on tissue context [48]. CD63 expression is also highly enriched in glioblastoma, a highly lethal malignancy of the astrocytes, and may play a role in progression of these cancers [49]. Our data hint that CD63 may play an important role in controlling cellular division through astrocyte-astrocyte cellular communication, which may represent an exciting new target for antitumoral agents.

Figure 4B shows a UMAP embedding of the gene embeddings learned by FIMP in an unsupervised manner during training. Each vector in the embedding table represents one gene in FIMP’s vocabulary of known genes, and genes with similar function or importance are expected to be closer together in the learned embedding space. Each gene in Figure 4B is colored by its average expression value across all astrocyte cells in the mouse hippocampus dataset. We see that the learned embeddings form distinct structures during training, and that highly-expressed genes for astrocytes are clustered together. We hypothesize that this ability to learn gene vectors in embedding space and contextualize them for different cell types allows FIMP to outperform other methods in gene expression prediction tasks.

### A.6 Attention Case Study 3: Word Interactions in Citation Networks

Given two nodes in a citation network, where nodes are represented by embedded BoW features, FIMP provides cross-attention matrices representing interactions between word features in neighboring nodes. To qualitatively assess the word feature interactions, we visualize four examples of cross-attention on the OGBN-arXiv dataset [50] in Figure

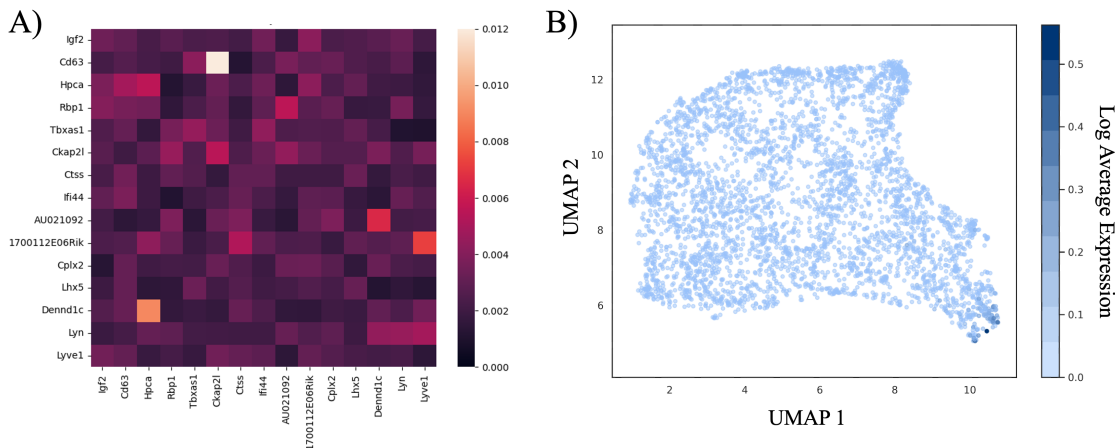


Figure 4: (A) Averaged attention between 15 genes across edges connecting neighboring astrocyte cells in the mouse hippocampus dataset. (B) UMAP of learned gene embeddings from FIMP, colored by average expression value of each gene across astrocyte cells.

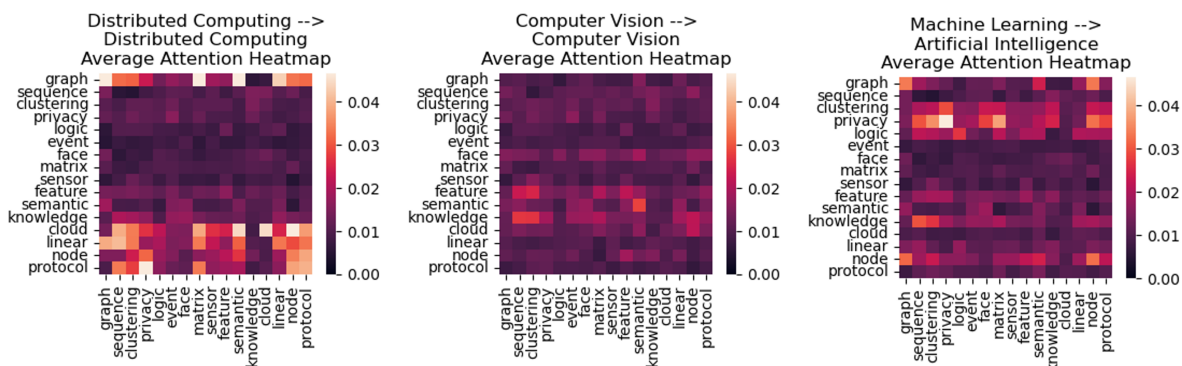


Figure 5: Averaged attention heatmap between the top 15 highly-attended words across four pairs of connected paper categories. Attention heatmaps are averaged across all edges connecting the pair of document categories. Rows represent word features of source nodes, and columns represent word features of the destination node on that edge.

5. Each heatmap is calculated by averaging attention heatmaps over all edges connecting that pair of computer science document categories. Note that because cross-attention is not completely symmetric, the feature interaction on edges passing information from one category to another might not be the same if the direction of the edge is reversed.

Intuitively, the feature interaction between two categories should highlight words which appear often in both categories of documents. We see in Figure 5 that a row-wise pattern emerges in the cross attention, where destination node features (columns) nearly all pay higher attention to a select few features in the source nodes. On self-edges between papers in the Distributed Computing category, we see words such as *graph*, *cloud*, and *protocol* highlighted, which often appear when describing distributed protocols. Self-edges between Computer Vision papers highlight completely different words, with *semantic* and *feature* receiving more attention by destination node features. On cross-category edges we see more spread in which words are highly-attended to, possibly because the set of common words between inter-category documents is more disjoint compared to intra-category documents.

We note that the feature-level interactions uncovered by FIMP depend highly on the identity of the features in the source and destination node, resulting in different highlighted features across edges when examining the same 15 words. We believe that this expressiveness in feature interaction benefits FIMP’s performance in tasks where feature interactions play important role in node-level or feature-level tasks.

### A.7 Hyperparameter Configurations

Hyperparameter tuning was done for all architectures on the fMRI reconstruction task, Slideseq-V2 and 10X human heart masked gene expression prediction tasks through a grid search over values for learning rate, weight decay, dropout, and attention dropout where applicable. Hidden dimension was set for each model to ensure an equal number of trainable parameters across different architectures to give all models equal capacity.

Table 5: Hyperparameters used on the fMRI recording reconstruction task.

	FIMP	GCN	GraphSAGE	GAT	GraphMAE	GPS GT	GIN
Trainable parameters	84988	86608	85520	86992	88020	86372	85328
Epochs	100	100	100	100	100	100	100
Learning rate	0.003	0.001	0.001	0.003	0.001	0.001	0.001
Dropout	0.0	0.0	0.0	0.0	N/A	0.0	0.0
Weight decay	1e-5	0.0	0.0	1e-5	1e-5	1e-5	0.0
Attention dropout	0.0	N/A	N/A	0.0	0.0	N/A	N/A

Table 6: Hyperparameters used on the Slideseq-V2 masked gene expression prediction task.

	FIMP	GCN	GraphSAGE	GAT	GraphMAE	GPS GT	GIN
Trainable parameters	314369	325680	317404	325840	333084	309544	329120
Epochs	200	200	200	200	200	200	200
Learning rate	0.003	0.003	0.01	0.01	0.01	0.01	0.01
Dropout	0.2	0.0	0.0	0.0	0.0	0.0	0.0
Weight decay	1e-5	1e-5	1e-5	0.0	0.0	1e-4	1e-5
Attention dropout	0.0	N/A	N/A	0.2	0.2	0.2	N/A

Table 7: Hyperparameters used on the 10X human heart masked gene expression prediction task.

	FIMP	GCN	GraphSAGE	GAT	GraphMAE	GPS GT	GIN
Trainable parameters	1284793	1309966	1309798	1166406	1330668	1214734	1312744
Epochs	200	200	200	200	200	200	200
Learning rate	0.01	0.001	0.003	0.001	0.01	0.01	0.003
Dropout	0.0	0.2	0.0	0.0	0.2	0.2	0.2
Weight decay	0.0	1e-5	0.0	1e-5	0.0	0.0	1e-5
Attention dropout	0.2	N/A	N/A	0.0	0.2	0.2	N/A